

NASA Technical Paper 1048

LOAN COPY: RETI  
AFWL TECHNICAL  
KIRTLAND AFB,



# An Experimental Evaluation of the Application of the Kirchhoff Formulation for Sound Radiation From An Oscillating Airfoil

Thomas F. Brooks

DECEMBER 1977





NASA Technical Paper 1048

An Experimental Evaluation  
of the Application of  
the Kirchhoff Formulation  
for Sound Radiation From  
An Oscillating Airfoil

Thomas F. Brooks  
Langley Research Center  
Hampton, Virginia



National Aeronautics  
and Space Administration

Scientific and Technical  
Information Office

1977



## CONTENTS

SUMMARY . . . . .	1
INTRODUCTION . . . . .	1
SYMBOLS . . . . .	2
THEORY . . . . .	5
MEASUREMENTS . . . . .	6
Description . . . . .	6
Experimental Procedure and Calibrations . . . . .	8
Results . . . . .	9
DISCUSSION OF RESULTS . . . . .	11
CONCLUSIONS . . . . .	13
APPENDIX A - THE KIRCHHOFF FORMULATION . . . . .	14
APPENDIX B - DERIVATION OF THEORETICAL MODEL . . . . .	17
APPENDIX C - ERROR ANALYSIS . . . . .	22
REFERENCES . . . . .	24
TABLES . . . . .	26
FIGURES . . . . .	28

## SUMMARY

The Kirchhoff integral formulation, which is often applied in aeroacoustic problems involving radiation from surfaces, is evaluated for its effectiveness in quantitatively predicting the sound radiated from an oscillating airfoil whose chord length is comparable with the acoustic wavelength. A rigid airfoil section was oscillated at small amplitude in a medium at rest to produce the sound field. Simultaneous amplitude and phase measurements were made of surface-pressure and surface-velocity distributions and the acoustic free field. Measured surface pressure and motion are used in applying the theory, and airfoil thickness and contour are taken into account. The result of the investigation was that theory overpredicted the sound pressure level by 2 to 5 dB, depending on direction. Differences were also noted in the sound-field phase behavior.

## INTRODUCTION

The determination of sound in a bounded region due to fluctuating loading acting over a boundary was first given by Kirchhoff (ref. 1) in his integral formulation of Huygens' principle. Curle (ref. 2) applied Kirchhoff's results to extend Lighthill's general theory of aerodynamic sound (ref. 3) to incorporate the influence of solid boundaries upon the sound field. Ffowcs Williams and Hawkings (ref. 4) generalized Curle's formulation to allow for arbitrary convective motion of a surface.

The aeroacoustic formulations have received wide application. However, in most practical problems of interest their use invariably involves assumptions in order to reduce the equations to tractable forms. A customary assumption for problems in which bodies - airfoils, in particular - encounter subsonic flow or undergo subsonic motions is that the linear surface terms of velocity and pressure dominate the production of the sound field, whereas the contributions from Lighthill's quadrupole term and that of surface viscosity are negligible in comparison (e.g., refs. 5 to 14). With this assumption the aeroacoustic equations reduce to Kirchhoff integral formulations.

The purpose of the present study is to examine experimentally the applicability of Kirchhoff's formulation in predicting the radiated sound from an airfoil undergoing a particular type of oscillatory motion. The study is motivated by the lack of definitive experimental data in the literature establishing directly that Kirchhoff's formulation provides the quantitative relationship between the linear surface terms and the acoustic field. Previous experimental studies of airfoil noise employing the theory (e.g., refs. 11 to 14) intrinsically involved factors which complicate the interpretation of the sound field, such as the presence of turbulent and sheared flow and complex distribution of surface pressure amplitude and phase. Also, the determination of the surface-pressure distribution has normally involved the use of airfoil theory rather than direct measurement. Such applications of the Kirchhoff formulation have

not always produced values that are in good quantitative agreement with the noise determined experimentally.

An experimental approach which provides a controlled method of investigating the relationship between surface-velocity and surface-pressure distributions and the resultant acoustic field is described herein. The noise source is a symmetrical airfoil section which is oscillated at small amplitudes about its center of gravity by a resonant vibratory system. To allow definitive comparison, tests were conducted in a stationary medium (no airflow), and only acoustic pure tones were generated by the body. For the two particular frequencies examined, 301 and 477 Hz, the 45.72-cm (18.0-in.) chord airfoil was not small compared with the acoustic wavelength. These frequencies were chosen because in typical aeroacoustic problems the frequencies of interest frequently correspond to wavelengths on the order of the chord length (see refs. 15 and 16).

Simultaneous amplitude and phase measurements were made of the velocity and pressure distributions on the airfoil surface and of the acoustic free field. The measured surface values of velocity and pressure are used in the theory, with airfoil thickness and contour taken into account, to predict the phase and amplitude of the acoustic free field. Differences are noted between the predicted and experimental values of the sound-field amplitude and phase.

#### SYMBOLS

Values are given in both SI Units and U.S. Customary Units. Measurements and calculations were made in U.S. Customary Units. Except when noted, surface and sound pressures are presented in decibels ( $\text{dB} = 20 \log (p_{\text{rms}}/p_{\text{ref}})$ , where  $p_{\text{ref}} = 20 \mu\text{Pa}$  ( $2 \times 10^{-4} \text{ dyn/cm}^2$ )).

b	airfoil semichord
c	speed of sound in fluid medium at rest
$F_i$	force per unit area exerted on fluid by solid boundary S in $x_i$ -direction
f	test frequency, Hz
G	density of volume source function internal to domain V
g	acceleration due to gravity
H	density of volume source function external to domain V
i	$= \sqrt{-1}$
$\hat{i}$	unit vector in $x_1$ - or $y_1$ -direction
$\hat{j}$	unit vector in $x_2$ - or $y_2$ -direction
k	wave number, $\omega/c$

$k_0, k_s, k_x$	see equation (B5)
$\hat{k}$	unit vector in $x_3$ - or $y_3$ -direction
$l$	semispan
$M_r$	component of Mach vector in direction of $\vec{r}$ , $\vec{r} \cdot \vec{v}/rc$
$\hat{n}$	unit normal vector to surface (drawn outward from surface into fluid)
$P_m$	specified complex surface pressure amplitude at element $m$
$p$	absolute pressure
$p_0$	mean value of pressure in medium
$p'$	gage pressure, $p - p_0$
$r$	$=  \vec{x} - \vec{y} $
$\vec{r}$	vector between observation point and source point, $\vec{x} - \vec{y}$
$S$	surface of body
SPP,SPV	see equation (7)
$T_{ij}$	Lighthill's stress tensor
$t$	observer time
$\vec{u}$	fluid velocity in the $\vec{y}$ -frame
$V$	volume region
$\vec{v}$	velocity of any point fixed in the $\vec{\zeta}$ -frame, $\partial \vec{y}(\vec{\zeta}, \tau) / \partial \tau$
$v_n$	surface normal velocity, $\vec{v} \cdot \hat{n}$
$\vec{x}$	observer position vector
$\vec{y}$	source position vector, $\vec{\zeta} + \int_0^\tau \vec{v}(\vec{\zeta}, \tau) d\tau$ (the $\vec{y}$ - and $\vec{\zeta}$ -frames are assumed to coincide at source time $\tau = 0$ )
$\alpha$	angular displacement of airfoil in oscillatory motion
$\beta$	sound-field directivity angle (see figs. 4 and B1)
$\delta$	Dirac delta function
$\delta_{ij}$	Kronecker delta ( $\delta_{ij} = 1$ for $i = j$ ; $\delta_{ij} = 0$ for $i \neq j$ )

$\epsilon$	unit height of airfoil segment (see fig. B1)
$\vec{\zeta}$	coordinate system affixed to body
$\eta$	slope of airfoil segment (see fig. B1)
$\tilde{\theta}$	angle between $\hat{n}$ and $\vec{r}$ (see fig. 1)
$\xi$	unit chord position of airfoil segment (see fig. B1)
$\rho$	instantaneous value of density
$\rho_0$	time-averaged value of density in medium
$\sigma_{ij}$	viscous stress tensor
$\tau$	emission time of source
$\Phi, \Psi$	scalar potentials
$\varphi_a$	phase angle of surface acceleration at leading edge
$\varphi_p$	phase angle of surface pressure
$\varphi_{sp}$	phase angle of sound pressure in acoustic field
$\omega$	angular frequency, rad/sec
$\nabla^2$	Laplacian operator, $\frac{\partial^2}{\partial y_1^2} + \frac{\partial^2}{\partial y_2^2} + \frac{\partial^2}{\partial y_3^2}$
$\vec{\nabla}_y$	differential operator, $\frac{\partial}{\partial y_1} \hat{i} + \frac{\partial}{\partial y_2} \hat{j} + \frac{\partial}{\partial y_3} \hat{k}$
[ ]	value within is taken at a retarded time $\tau = t - \frac{r}{c}$

Subscripts:

b	bottom of airfoil segment (see fig. B1)
i, j	components of a vector or summation indices
m	particular element of the airfoil equivalent model (see fig. B1)
ref	constant reference value
rms	root-mean-square value
t	top of airfoil segment (see fig. B1)

## THEORY

The aerodynamic sound generated from a region which includes rigid surfaces in arbitrary convective motion is given by Ffowcs Williams and Hawkings in reference 4. The solution relates the air density fluctuation  $\rho - \rho_0 = \rho(\vec{x}, t) - \rho_0$  at position  $\vec{x}$  and time  $t$  in terms of space and time derivatives of surface and volume integrals over source region  $\vec{y}$ . For the coordinate system shown in figure 1, the solution is (from ref. 4)

$$4\pi c^2(\rho - \rho_0) = \frac{\partial}{\partial x_i} \frac{\partial}{\partial x_j} \int_V \left[ \frac{T_{ij}}{r|1 - M_r|} \right] dV(\vec{\zeta}) - \frac{\partial}{\partial x_i} \int_S \left[ \frac{F_i}{r|1 - M_r|} \right] dS(\vec{\zeta}) + \frac{\partial}{\partial t} \int_S \left[ \frac{\rho_0 v_n}{r|1 - M_r|} \right] dS(\vec{\zeta}) \quad (1)$$

In the volume integral,  $T_{ij}$  is Lighthill's fluid stress tensor related by

$$T_{ij} = \rho u_i u_j + \delta_{ij} [(p - p_0) - c^2(\rho - \rho_0)] - \sigma_{ij} \quad (2)$$

The Reynolds stress term  $\rho u_i u_j$  is usually taken as  $\rho_0 u_i u_j$  for low Mach number flow. The term  $\delta_{ij} [(p - p_0) - c^2(\rho - \rho_0)]$  represents the effect of heat conduction, which is considered very small for low Mach number flow. The term  $\sigma_{ij}$  is the viscous stress tensor.

In the surface integrals, the surface force per unit area  $F_i$  is given by

$$F_i = n_i(p - p_0) - n_j \sigma_{ij} \quad (3)$$

where  $n_i$  is the  $i$ th component of  $\hat{n}$ , which is the unit surface normal (positive from surface into the fluid). The term  $v_n$  is the normal surface velocity.

Equation (1) reduces to that obtained from Curle's analysis (ref. 2) when surface convection is not a factor. Equation (1) is regarded as a complete and exact description of the sound field.

The application of equation (1) to determine the sound produced for a particular problem invariably involves assumptions, because the required flow parameters normally can only be specified to a limited extent. Consider a slender body, such as an airfoil section, producing sound due to its own motion and/or its reaction to an encounter with a complicated subsonic flow pattern. An important assumption for many applications is that the sound is dominated by that produced by the net local force on the body and the motion of the body. The primary argument used to justify this assumption for particular cases is that the quadrupole-type noise source mechanism, represented by the volume integral of equation (1), is less efficient than the dipole- and monopole-type mechanisms, as represented in the surface integrals.

If, in addition to ignoring the contribution of the volume integral, one also neglects in equation (1) the viscous components of the surface force, then the sound field may be described by the following equation:

$$4\pi p'(\vec{x}, t) = 4\pi [p(\vec{x}, t) - p_0]$$

$$= \frac{1}{c} \frac{\partial}{\partial t} \int_S \left[ \frac{\rho_0 c v_n + p' \cos \tilde{\theta}}{r |1 - M_r|} \right] dS(\vec{\zeta}) + \int_S \left[ \frac{p' \cos \tilde{\theta}}{r^2 |1 - M_r|} \right] dS(\vec{\zeta}) \quad (4)$$

as shown by Farassat (ref. 9). In equation (4),  $p'(\vec{x}, t)$  is the acoustic pressure at the observer; within the integrals,  $p' = p(\vec{\zeta}, \tau) - p_0$  is the surface "gage" pressure.

If the surface is stationary or is undergoing solid-body vibratory motion of small amplitude, where  $|v_n| \ll c$ , equation (4) may be simplified to

$$4\pi p'(\vec{x}, t) = \frac{1}{c} \frac{\partial}{\partial t} \int_S \frac{\rho_0 c [v_n] + [p'] \cos \tilde{\theta}}{r} dS(\vec{y}_{avg}) + \int_S \frac{[p'] \cos \tilde{\theta}}{r^2} dS(\vec{y}_{avg}) \quad (5)$$

where  $\vec{y}_{avg}$ , the average value of source coordinate  $\vec{y}(\vec{\zeta}, \tau)$ , coincides with the  $\vec{\zeta}$ -coordinate affixed to the body. Equation (5) is Kirchhoff's integral formula. (See appendix A.)

## MEASUREMENTS

### Description

Apparatus.— A sketch of the experimental airfoil model is shown in figure 2. The rigid symmetrical NACA 0012 aluminum airfoil section (thickness-to-chord ratio of 0.12) had a chord of 45.72 cm (18.0 in.) and a span of 30.48 cm (12.0 in.). The airfoil was part of a resonant torsional vibration system which also included torsional bars with inertia disks. The system was designed to produce a sinusoidal oscillation of controllable amplitude about the center of gravity of the airfoil section, located 19.05 cm (7.50 in.) from the leading edge of the airfoil. As illustrated in figure 2, the vibrational mode used was such that the torsional motion at the two disks was 180° out of phase with the rigid-airfoil rotational motion. This mode was generated and maintained by input supplied at one of the inertia disks by an ordinary shaker unit (15.2 cm (6.0 in.) in diameter and 15.2 cm long) whose amplitude and frequency were controlled by a frequency generator and a power supply.

For the tests two sets of 27.94-cm (11.0-in.) long torsional bars with inertia disks having diameters of 30.48 cm (12.0 in.) and 19.38 cm (7.63 in.) were used, and each produced the described mode at different tuning frequencies, which were respectively 301 Hz and 477 Hz. A photograph of the experimental model in the 301-Hz configuration is shown in figure 3. Pretest accelerometer surveys verified the mode shape of the sinusoidal motion.

The tests were conducted in the Langley anechoic noise facility. The chamber is approximately 7.6 m (25 ft) long, 7.6 m (25 ft) wide, and 7.0 m (23 ft) high. Figure 4 shows the airfoil test assembly suspended from the ceiling in the chamber. The center of the airfoil span was positioned 1.83 m (6.0 ft) from the acoustic wedges of the floor and about 2.1 m (7 ft) from the wedges of the

nearest wall. The shaker was connected to the airfoil assembly by a small-diameter steel rod secured at the shaker armature and at an off-center position on the inertia disk. In addition to transmitting the sinusoidal input (lateral rod displacement on the order of typically  $10^{-3}$  cm) to the resonant vibratory system, the placement of the rod prevented assembly misalignment and sway from its vertical position.

Instrumentation.- A 2-g (0.0643-oz) piezoelectric accelerometer was used to determine the rigid-airfoil motion. The accelerometer was mounted in an instrument module and positioned 4.92 cm (1.94 in.), measured chordwise, from the leading edge. All wiring from the module led out of the test assembly through the center of a torsional bar in such a way as to minimize extraneous signal noise due to vibration.

To measure the sound field, fourteen 0.635-cm (0.25-in.) diameter and two 1.27-cm (0.5-in.) diameter, standard condenser free-field microphones were used. The 16 microphones were positioned on a 2.44-m (8-ft) radius microphone boom. As shown in the plan view of figure 4, the microphones were placed at  $12^\circ$  increments to cover a range of directivity angle  $\beta$  of  $180^\circ$ . Care was taken to position the microphone diaphragm in the plane perpendicular to the airfoil surface at the midspan within 1.3 cm (0.5 in.) and at a 2.210-m (7.25-ft) radius from the airfoil center of oscillation within 0.3 cm (1/8 in.).

The airfoil surface-pressure distribution was determined with piezoresistive silicon pressure transducers (ref. 17). The devices were chosen because of their low acceleration sensitivity, small size, and excellent long-term sensitivity and phase stability. The 0.3175-cm (1/8-in.) diameter diaphragm of the transducer has its first resonant frequency at 70 kHz, and with a 10-V dc excitation voltage, the transducer sensitivity is  $-117$  dB(ref. 1 V)/Pa.

Eight fixed-position transducers and one variable-position transducer measured the surface pressure. On one side of the symmetrical airfoil, the fixed transducers were flush mounted on the instrument module. These transducers were located 3.175 cm (1.25 in.) from the midspan and were positioned at 1.4, 9.7, 21.2, 31.9, 48.6, 61.8, 78.1, and 88.9 percent of the chord, measured from the leading edge (chord length: 45.72 cm (18.0 in.)).

The spanwise surface-pressure distribution was examined by a transducer cemented to a thin steel plate which, in turn, was bonded at each chosen position. As a result of this surface-mounting technique, the transducer diaphragm was elevated 0.318 cm (1/8 in.) above the airfoil surface. Although this elevation precluded direct surface-pressure measurement, the spanwise distribution of surface pressure amplitude and phase was accurately determined by referencing data obtained to values measured at flush-mounted transducer locations. The movable transducer was positioned along the span in line with the 21.2-, 78.1-, and 88.9-percent-chord flush-mounted transducer locations. These positions were at 10.4, 25.0, 33.3, and 41.7 percent of the span, measured from the span center line. The 10.4-percent-span positions (3.175 cm (1.25 in.) from the midspan) were spanwise symmetrical to the flush-mounted transducer locations. An additional position employed was along the line of the flush-mounted transducer at locations 97.2 percent of the chord, measured from the leading edge.

## Experimental Procedure and Calibrations

Instrument calibrations.- For the surface-pressure transducers the output voltage signal  $e$  is the sum of the combined signals due to pressure  $p$  and acceleration  $a$  at the diaphragm. The voltage output ratio is

$$\frac{e}{e_{\text{ref}}} = \frac{S_p p + S_a a}{S_p p_{\text{ref}}} = \frac{p}{p_{\text{ref}}} + \frac{S_a a}{S_p p_{\text{ref}}} \quad (6)$$

where  $p$  and  $a$ , and thus  $e$ , are complex quantities, with the amplitude and phase dependent on experimental conditions. The reference voltage  $e_{\text{ref}}$  is determined by a chosen reference pressure  $p_{\text{ref}}$ . The value of the ratio  $S_a/S_p$  has been determined by a two-part laboratory calibration on a random sample of four pressure transducers. The pressure sensitivity  $S_p$  was found by an acoustic calibration, and the acceleration sensitivity perpendicular to the diaphragm plane  $S_a$  was determined for the transducers in a vacuum (an atmospheric pressure of 667 Pa (5 mm Hg)).

A range of conditions was considered up to a frequency of 2 kHz, up to an rms acceleration level of 15g, and up to a sound pressure level of 150 dB. The average value of  $S_a/S_p$  was 0.506 (mV/g)/(mV/Pa) with a standard deviation of 0.069. The value was independent of frequency and levels of acceleration and pressure.

In addition to the instrumentation-laboratory calibration for the surface-pressure transducers, on-site amplitude and phase calibrations were conducted for the accelerometer, microphones, and surface-pressure transducers prior to and during the data acquisition period. The calibration instruments included a 100-Hz, 1g<sub>rms</sub> vibration calibrator, a 114-dB sound-level calibrator, and a microphone-transducer acoustic calibrator whose calibration frequency is determined by a frequency generator. The outputs of these calibrators as a function of frequency and sound level were compared with the outputs of several calibrators of different types, and agreement was found.

The accelerometer signal was determined to be in phase with the acceleration. Routine amplitude calibrations incorporated a substitute accelerometer of the same type. Cross calibrations were made between the accelerometer and its substitute at the beginning and end of the test program.

The signals from the surface-pressure transducers were found to be in phase with the pressure and acceleration variations. The transducers were phase matched within 1° at both 301 Hz and 477 Hz. Amplitude calibrations were conducted prior to each series of tests for 301 Hz and 477 Hz at 120 dB. No measurable change occurred in the pressure-transducer calibration during the experimental study.

Because of the condenser-microphone and preamplifier circuitry, the signals from the microphones were inverted with respect to the acoustic pressure at the diaphragms. The phase calibrations, which incorporated the same acoustic calibrator used for the surface-pressure transducers, showed that the microphones were phase matched within a standard deviation of 2.3° for 301 Hz and within a

standard deviation of  $6.2^\circ$  for 477 Hz. The routine 114-dB amplitude calibrations revealed less than a 0.25-dB variation in the calibrations for any one microphone.

Anechoic chamber calibration.- The quality of the acoustic field was examined for the two pure-tone frequencies of interest with the use of an apparatus (ref. 18) which simulates an ideal acoustic point source. The source emission of the apparatus is from a small-diameter opening of a necked-down tube.

For the tests the airfoil assembly and shaker were removed from the chamber and the acoustic driver of the calibrator apparatus was secured to the shaker stand. The source was positioned in the center of the vacated airfoil assembly region, equidistant to the 16 microphones. The results of the test are shown in figure 5, where the directivity of the source as found by the microphones is plotted in terms of sound pressure level and phase against microphone position (the angle  $\beta$ ). The phase was determined by referencing the microphone signals to the acoustic driver input signal. The deviation shown from the mean values of sound pressure level and phase indicates the quality of the acoustic field.

The results show anechoic behavior for the test frequencies within  $\pm 1$  dB sound pressure level and  $\pm 12^\circ$  phase (except for results of one microphone). The flagged symbols indicate that the phase was unstable for the microphone at  $\beta = 132^\circ$ . The data for the microphone at  $\beta = 156^\circ$  are not included in figure 5 because the microphone was replaced during the experimental program.

Data acquisition and reduction.- For the tests the sinusoidal signals from all instruments were appropriately conditioned for recording on a 14-track FM analog tape recorder which was operated such that it had a flat frequency response up to 10 kHz.

The primary instruments used to reduce the recorded calibration and experimental data were two graphic level recorders and a phase meter. To enhance stability of the phase measurements, it was found convenient to employ two matched dynamic tracking filters. The frequency was tuned by the accelerometer signal and the frequency bandwidth used was 20 Hz. The accelerometer signal was used to determine the motion of the rigid airfoil section and also as a phase reference for all pressure transducer and microphone signals. Determination of the surface pressure amplitude and phase incorporated the use of equation (6).

## Results

Surface-pressure and airfoil-motion measurements.- Four cases are considered. For a frequency of 301 Hz, the test airfoil-section motion produced rms accelerations of 2.99g and 9.44g at the accelerometer location. These accelerations correspond, respectively, to peak angular displacements  $\alpha$  of 82.1  $\mu$ rad and 259.3  $\mu$ rad. For a frequency of 477 Hz, the rms accelerations were 2.82g and 8.91g, which correspond to  $\alpha$  values of 30.8  $\mu$ rad and 97.6  $\mu$ rad, respectively. For reference it is noted that the maximum oscillatory displacement was located at the trailing edge, where the rms value was 0.049 mm ( $1.93 \times 10^{-3}$  in.) for the 9.44g case. Thus the maximum oscillatory velocity corresponds to

a velocity of 0.131 m/s (0.429 ft/sec), which meets stated requirements for the validity of equation (5).

The results for the eight flush-mounted pressure transducers are given in table 1. Presented are the surface pressures and the phases by which the sinusoidal pressures lead the surface acceleration of the leading-edge region, denoted by  $\phi_p - \phi_a$ . These results are also presented in figure 6, where the levels of the rms surface pressures are given in decibels. Also shown in figure 6 are additional measurement values at the movable transducer position near the trailing edge at 97.2 percent of the chord.

It is seen that for both 301 and 477 Hz, the surface pressure amplitude varies in approximate proportion to, and is approximately in phase with, the surface acceleration (positive as directed from the surface into the medium). The surface-pressure chordwise distributions are smooth and have minimum values and maximum phase change near the center of the sinusoidal oscillation (at 41.7 percent of the chord).

The results of the spanwise pressure survey for a 477-Hz case are shown in figure 7. As previously discussed, the levels from the slightly elevated movable transducer are referenced to values measured at flush-mounted transducer locations. The pressure phase is invariant over the span, whereas the pressure level is essentially uniform over most of the span. The surface pressure diminishes in level as the edge of the airfoil section is approached.

Predictions of the acoustic field and comparisons with experimental values.- The measured values of surface pressure and velocity may be used in the theory, as represented by equation (5), to predict the acoustic field for comparison with the experimental values. Sufficient information is known to evaluate equation (5) accurately, because the pressure amplitudes on the side of the airfoil not containing pressure transducers are identical with values obtained from the instrumented side, but the phase of the pressure is shifted by  $180^\circ$ . This is true because of airfoil geometric symmetry, motion antisymmetry, and the fact that all measured quantities (motion, surface pressure, and sound pressure) were sinusoidal with no discernible harmonics.

The contour of the actual experimental model is approximated by plane segments (see figs. 8(a) and (b)). Because of airfoil symmetry, the corresponding segments on each side of the airfoil can be considered simultaneously in the calculations. The amplitude and phase of the surface pressure are considered uniform over the segments, whereas the chordwise dependence for velocity is taken into account for each segment. In using equation (5) to develop the model, the orientation and position of the surface with regard to an observer in the sound field are accurately defined.

The airfoil equivalent model as shown in figure 8(b) is comprised of eight elements that radiate independently, which is consistent with the integral form of equation (5). For an observer in the far field of each individual element, equation (5) becomes

$$p'(\vec{x}, t) = SPV + SPP = \sum_{m=1}^8 (SPV)_m + (SPP)_m \quad (7)$$

where

$$(SPV)_m = \frac{1}{4\pi} \frac{\partial}{\partial t} \int_{S_m} \frac{\rho_o [v_n]}{r} dS \quad (8)$$

and

$$(SPP)_m = \frac{1}{4\pi c} \frac{\partial}{\partial t} \int_{S_m} \frac{[p'] \cos \tilde{\theta}}{r} dS \quad (9)$$

where the small contribution from the last integral of equation (5) has been excluded (see appendix B). The symbols SPV and SPP are complex quantities and are respectively the sound pressure due to the surface-velocity term and that due to the surface-pressure term.

Details of the evaluation of  $(SPV)_m$  and  $(SPP)_m$  are contained in appendix B. Far-field approximations for each element  $m$  are employed; however, the summation procedure rendering  $p'(\vec{x}, t)$  represents a numerical integration in which the far field of the airfoil itself is not assumed.

The prediction of the acoustic field for each experimental case is determined by using equation (7) with the values of  $(SPV)_m$  and  $(SPP)_m$  obtained from equations (B8) and (B9), respectively. The experimental results contained in table 1 and the airfoil section geometric constants and the physical constants in table B1 are used to evaluate equations (B8) and (B9).

In figures 9 and 10 are presented the noise data that were measured simultaneously with the surface pressures and accelerations given in figure 6 (also table 1). Presented are the sound pressure levels and corresponding phases by which the sinusoidal sound pressures lead the airfoil-surface acceleration at the leading-edge region, denoted by  $\varphi_{sp} - \varphi_a$ , as a function of the directivity angle  $\beta$ . All data are for measurement locations in the plane bisecting the midspan of the airfoil section at a radius of 2.210 m (7.25 ft) from the center of oscillation.

Also included in figures 9 and 10 are the corresponding theoretical predictions determined from equation (7) by using the experimental data from table 1. All theoretical levels include a negative 0.7-dB adjustment to account for the spanwise-diminished surface pressure levels near the airfoil-section edges (see fig. 7).

#### DISCUSSION OF RESULTS

It is seen that for both 301 Hz (fig. 9) and 477 Hz (fig. 10), the theoretically predicted acoustic levels are higher than those measured by some 2 to 5 dB, depending on directivity angle  $\beta$ . The closest agreements appear near  $\beta = 90^\circ$ , where it is noted the sound pressure would be expected to be determined for the

most part by the total fluctuating airfoil lift, since the retarded times for all parts of the airfoil are approximately equal for the measurement position.

Of equal significance to sound pressure level for evaluation of the theoretical-experimental comparison are the phase values. For all cases agreement may be considered acceptable near  $\beta = 90^\circ$ . However for 301 Hz at  $\beta$  ranging from  $12^\circ$  to  $132^\circ$ , the theoretical change in phase is about  $30^\circ$  larger than the measured change. For 477 Hz at the same  $\beta$  range, the theoretical change in phase is about  $50^\circ$  larger than the measured change.

Note that the results for the microphone at  $\beta = 156^\circ$  were not included in the acoustic field calibration (see fig. 5). Therefore, no conclusions may be drawn on the basis of the data points for this value of  $\beta$ .

In view of the disagreement between the theoretical and experimental results, an error analysis was performed (see appendix C). The error analysis indicated that the experimental noise data of figures 9 and 10 should be accurate within  $\pm 1$  dB in sound pressure level and about  $\pm 12^\circ$  in phase for at least 14 of the 16 microphones. However, because of the number of independent measuring systems, only a smaller net error could result in the overall directivity determination of sound pressure level and phase.

The accuracy of the theoretically predicted curves of figures 9 and 10 is dependent on that of the surface measurements and the theoretical model. On the basis of a cumulative component analysis, with allowances for possible experimental procedural error, an ample error band to assign these curves should be  $\pm 1.5$  dB in level and  $\pm 15^\circ$  in phase.

From the results of the error analysis, it is concluded that for the case considered, the Kirchhoff solution did not accurately render the quantitative relationship between the surface-velocity and surface-pressure distributions and the resultant acoustic field.

It is of interest to note that this same trend of overpredicting the sound has been found in other quantitative studies, which involved an analogous problem of noise from stationary airfoils encountering turbulent flow, as shown in references 11 and 12. In contrast, good quantitative results were obtained in studies of noise of high-tip-speed rotors (refs. 13 and 14), where the solution of Kirchhoff's problem for surfaces in convective motion was employed using normal surface-velocity distributions and calculated steady-loading distributions (unsteady loading being ignored).

This experimental study tests suitability of Kirchhoff's formulation for a particular application; therefore the results cannot be generalized for all aeroacoustic applications involving surfaces. The tests were conducted for only two frequencies, whose acoustic wavelengths were comparable with the chord length, and for only one type of oscillatory airfoil motion. Also, as pointed out in reference 11, there are significant conceptual differences in the noise produced by surface motion and that produced from a stationary surface opposing fluid motion, although the same aeroacoustic theory embodies both. The results do, however, serve to question the usefulness of normal surface-pressure measure-

ments used in Kirchhoff's formulation to predict noise accurately for arbitrary situations involving surface-flow interaction.

A natural inclination may be to consider that the neglect of viscous effects in the Kirchhoff formulation should not give rise to as much disagreement as shown in the results. However in another respect the surface-pressure data (fig. 6) suggest that viscous effects may not be negligible. The pressure loadings appear to approach constant levels at the edges rather than tending to zero. This behavior is consistent with that found in some recent studies of unsteady aerodynamics (refs. 19 and 20) demonstrating failure of the classical Kutta-Joukowski condition at the edges of airfoils operating at high reduced frequency. Such discrepancies, as explained in reference 21, may be due to linear viscous effects. If it is indeed true that one must consider airfoil theory for unsteady, viscous flow to describe the surface-pressure distribution properly, then it may be suggested that one should not ignore viscosity in the prediction of the sound field.

### CONCLUSIONS

For a particular rigid body undergoing vibratory motion, the quantitative relationship between surface-velocity and surface-pressure distributions and the resultant acoustic free field was examined and compared with that predicted from the Kirchhoff integral formulation.

To allow definitive comparison for pressure levels and phase, the acoustic data generated were pure tone and the tests were conducted in a stationary medium (no airflow). A symmetrical airfoil section was oscillated at small amplitudes at two frequencies: 301 and 477 Hz. These frequencies correspond to values of the compressible frequency parameter (wave number times airfoil semichord) of 1.3 and 2.0.

The theory was applied by using measured airfoil surface pressure and motion to predict the sound field, which was compared with experimental values. It was found that for both test frequencies,

1. The applied theory overpredicts the measured sound pressure level by 2 to 5 dB, depending on directivity angle.
2. The phase variation, over a large range of directivity angle, is over-predicted by the theory.
3. The closest overall agreement for sound pressure level and phase appears near the directivity angle which corresponds to a location perpendicular to the airfoil chord line. However, even here differences are significant.

Langley Research Center  
National Aeronautics and Space Administration  
Hampton, VA 23665  
October 31, 1977

## APPENDIX A

### THE KIRCHHOFF FORMULATION

This appendix gives a summary of the derivation of a solution to the inhomogeneous scalar wave equation. This solution contains the surface integral known as Kirchhoff's integral formulation of Huygens' principle, which is shown to be equivalent to equation (5), the equation applied in this experimental study.

Consider the sound inside a given domain as being determined by the sound sources inside this domain and by sound which enters from the outside. Mathematically, one relates the sound field to its sources by integrating an inhomogeneous differential equation. Let  $\Psi$  represent a scalar potential, let  $G(\vec{y}, t)$  be the density of the source function internal to a domain  $V$ , and let  $H(\vec{y}, t)$  be the density of the source function external to domain  $V$ . It is assumed that throughout the domain  $V$ , the medium containing the source  $G(\vec{y}, t)$  is homogeneous and isotropic and contains no surfaces which would reflect or scatter sound waves. Within domain  $V$  the scalar function  $\Psi$  satisfies the equation

$$\nabla^2 \Psi - \frac{1}{c^2} \frac{\partial^2 \Psi}{\partial t^2} = -G(\vec{y}, t) \quad (\text{A1})$$

where  $c$  is the speed of sound.

Let domain  $V$  be closed and bounded by a regular surface  $S$  and let  $\Phi$  and  $\Psi$  be any two scalar potentials whose first and second derivatives are continuous throughout  $V$  and on  $S$ . Given this, Green's integral is valid:

$$\int_V (\Psi \nabla^2 \Phi - \Phi \nabla^2 \Psi) dV = \int_S \left( \Phi \frac{\partial \Psi}{\partial n} - \Psi \frac{\partial \Phi}{\partial n} \right) dS \quad (\text{A2})$$

where  $\partial/\partial n$  denotes differentiation along the normal to  $S$  (normal positive into  $V$ ). Let  $\vec{x}$  be a fixed observation point within  $V$  and

$$r = \sqrt{(x_1 - y_1)^2 + (x_2 - y_2)^2 + (x_3 - y_3)^2} \quad (\text{A3})$$

be the distance of the fixed point from a variable point  $\vec{y}$ . (See fig. A1.)

In equation (A2),  $\Psi$  is identified with the desired solution of the wave equation (A1). The function  $\Phi$  is taken as a function relating the result in the field at  $\vec{x}$  due to an activity at  $\vec{y}$ .

The Kirchhoff theory of integration is used to obtain  $\Psi$  (e.g., refs. 1 and 22 to 25) from the wave equation (A1), the prescribed conditions of continuity (eq. (A2)), and a choice of function  $\Phi$ . To allow the desired solution, function  $\Phi$  is conveniently taken as the elementary solution of the homogeneous equation

APPENDIX A

$$\nabla^2 \Phi - \frac{1}{c^2} \frac{\partial^2 \Phi}{\partial t^2} = 0 \quad (\text{A4})$$

which is

$$\Phi = \frac{A}{r} \delta\left(t - \frac{r}{c}\right) \quad (\text{A5})$$

This is the free-field Green's function (see ref. 7), where  $A$  is an arbitrary constant,  $t$  is time, and  $\delta$  is the Dirac delta (or impulse) function. The result is the solution to the inhomogeneous scalar wave equation (A1), also known as the Kirchhoff formula,

$$\Psi(\vec{x}, t) = \frac{1}{4\pi} \int_V \frac{1}{r} [G] dV + \frac{1}{4\pi} \int_S \left\{ [\Psi] \frac{\partial}{\partial n} \left( \frac{1}{r} \right) - \frac{1}{cr} \frac{\partial r}{\partial n} \left[ \frac{\partial \Psi}{\partial t} \right] - \frac{1}{r} \left[ \frac{\partial \Psi}{\partial n} \right] \right\} dS \quad (\text{A6})$$

where the symbol  $[G] = G\left(\vec{y}, t - \frac{r}{c}\right)$  denotes a function taken at retarded time  $\tau = t - \frac{r}{c}$ .

In equation (A6) the volume integral is a particular solution of the inhomogeneous wave equation which physically represents the contribution of all sources  $G$  contained within  $V$ . The surface integral is a general solution of the homogeneous equation (A4), where the integral extends over  $S$  and accounts for all sources  $H$  located outside  $V$ .

The Kirchhoff formula can be applied for an infinite region  $V$  containing the observer point  $\vec{x}$  and bounded internally by a closed surface  $S$ . The restriction formerly introduced - that the surface of integration is a closed surface containing  $\vec{x}$  - is satisfied by assuming that a portion of the surface is displaced to infinity, where its contribution to the integral is zero. (See fig. A2.) Such a procedure is valid whenever the Sommerfeld condition is satisfied, that is, when the product  $\Psi r$  is less than some constant, which is always the case for the acoustic phenomena considered here.

In reference 2, Curle employed equation (A6) and the Lighthill formulation of aerodynamic sound to determine the influence of solid boundaries upon the sound field.

The surface integral of equation (A6) is what may be described as Kirchhoff's integral formulation of Huygens' principle, as seen in reference 1. In equation (A6), if one lets  $\Psi$  equal the velocity potential, noting that the acoustic pressure  $p'(\vec{x}, t) = c^2(\rho - \rho_0) = \rho_0 \partial \Psi / \partial t$  and velocity  $v_n = (-\vec{\nabla}_y \Psi) \cdot \hat{n} = -\frac{\partial \Psi}{\partial n}$ , then one obtains

$$4\pi p'(\vec{x}, t) = \frac{1}{c} \frac{\partial}{\partial t} \int_S \frac{\rho_0 c [v_n] + [p'] \cos \tilde{\theta}}{r} dS + \int_S \frac{[p'] \cos \tilde{\theta}}{r^2} dS \quad (\text{A7})$$

## APPENDIX A

where in the integrals,  $p'$  is the surface gage pressure and

$$\cos \tilde{\theta} = -\hat{n} \cdot \vec{\nabla}_y r = -\frac{\partial r}{\partial n}$$

which is the cosine of the angle between the surface normal and vector  $\vec{r} = \vec{x} - \vec{y}$  (see fig. 1). Equation (A7) is identical with equation (5) and, except for the omission of convective effects, is that found by Farassat in reference 9.

## APPENDIX B

### DERIVATION OF THEORETICAL MODEL

The purpose of this appendix is to show the derivation of the velocity term  $(SPV)_m$  and the pressure term  $(SPP)_m$  for the theoretical model used for the prediction of the acoustic field in the experimental section.

Each of the radiating elements illustrated in figure 8(b) is approximated by straight plane segments of which the cross section and its coordinate system are shown in figure B1. In this figure the origin represents the pivotal point of the rigid-airfoil vibration, and the observer at position  $\vec{x}$  is at a constant radius  $r_0$  from the origin and is at an angle  $\beta$  with respect to the  $x_2$ -axis. The observer remains in the  $x_2$ - $x_3$  plane.

In figure B1 the two segments representing the element  $m$  are denoted as top and bottom. The coordinate  $y_3$  is given by

$$y_3 = b[\varepsilon - \eta(\xi - \xi_0)]$$

for the top segment and by

$$y_3 = -b[\varepsilon - \eta(\xi - \xi_0)] \quad (\xi_1 \leq \xi \leq \xi_2) \quad (B1)$$

for the bottom segment. Here

- b            semichord of the airfoil
- $\xi$            unit position on  $y_2$ -axis,  $y_2/b$
- $\eta$            slope of segment  $m$
- $\varepsilon$         unit height,  $y_3/b$ , at center of segment  $m$

The normal  $\hat{n}_t$  for the top segment is

$$\hat{n}_t = \frac{\eta}{\sqrt{1 + \eta^2}} \hat{j} + \frac{1}{\sqrt{1 + \eta^2}} \hat{k}$$

whereas for the bottom segment one obtains

$$\hat{n}_b = \frac{\eta}{\sqrt{1 + \eta^2}} \hat{j} - \frac{1}{\sqrt{1 + \eta^2}} \hat{k}$$

The surface velocity  $v_n$  in equation (8) for element  $m$  has linear variation in the  $y_2$ -direction. The prescribed sinusoidal velocity is

$$v_t = i\omega ab \exp i\omega t \left\{ [\varepsilon - \eta(\xi - \xi_0)] \hat{j} + \xi \hat{k} \right\}$$

APPENDIX B

for the top and

$$v_b = i\omega ab \exp i\omega t \left\{ -[\epsilon - \eta(\xi - \xi_0)] \hat{j} + \xi \hat{k} \right\}$$

for the bottom, where  $\alpha$  is the angular displacement. The surface pressure  $p'$  in equation (9) is assumed to be uniform and sinusoidal over each segment. For the top segment of element  $m$ ,  $p' = P_m \exp i\omega t$ , and for the bottom segment,  $p' = -P_m \exp i\omega t$ , because of symmetry of the airfoil and antisymmetry of the surface motion. The term  $P_m$  is a complex quantity in order to allow phase specification between pressure and surface motion. For the top segment the normal velocity  $v_n$  is

$$v_{n,t} = \vec{v} \cdot \hat{n}_t = i\omega ab \xi \exp i\omega t \left\{ \frac{1 + \frac{\eta}{\xi} [\epsilon - \eta(\xi - \xi_0)]}{\sqrt{1 + \eta^2}} \right\}$$

and, correspondingly for the bottom segment,

$$v_{n,b} = \vec{v} \cdot \hat{n}_b = -v_{n,t}$$

For the integrals of equations (8) and (9) the differential surface area for the element  $m$  is  $dS = dy_1 \sqrt{1 + \eta^2} dy_2 = dy_1 b \sqrt{1 + \eta^2} d\xi$ . The coordinate  $y_1$  varies from  $-\ell$  to  $\ell$ , where  $\ell$  is the semispan of the airfoil. The following is obtained for equation (8):

$$\begin{aligned} (SPV)_m = & \frac{-\rho_0 b^2 \omega^2 \alpha}{4\pi} \int_{-\ell}^{\ell} \int_{\xi_1}^{\xi_2} \left[ \xi(1 - \eta^2) + \eta(\epsilon + \eta\xi_0) \right] \left\{ \frac{\exp \left[ i\omega \left( t - \frac{r_t}{c} \right) \right]}{r_t} \right. \\ & \left. - \frac{\exp \left[ i\omega \left( t - \frac{r_b}{c} \right) \right]}{r_b} \right\} d\xi dy_1 \end{aligned} \quad (B2)$$

Equation (9) becomes

$$\begin{aligned} (SPP)_m = & \frac{ib\omega P_m \sqrt{1 + \eta^2}}{4\pi c} \int_{-\ell}^{\ell} \int_{\xi_1}^{\xi_2} \left\{ \frac{\cos \tilde{\theta}_t \exp \left[ i\omega \left( t - \frac{r_t}{c} \right) \right]}{r_t} \right. \\ & \left. - \frac{\cos \tilde{\theta}_b \exp \left[ i\omega \left( t - \frac{r_b}{c} \right) \right]}{r_b} \right\} d\xi dy_1 \end{aligned} \quad (B3)$$

The radii  $r_t$  and  $r_b$  are respectively the distance from the differential area  $dS$  of the top and  $dS$  of the bottom segment to the observer at  $\vec{x}$ . The angle  $\tilde{\theta}_t$  is the angle between the normal at  $dS$  for the top segment and the radius  $r_t$ . Correspondingly,  $\tilde{\theta}_b$  is the angle between the normal for the bottom segment and  $r_b$ .

From the coordinate system illustrated in figure B1, the center of element  $m$  at  $\xi = \xi_0 = (\xi_1 + \xi_2)/2$  is at a radius  $r_m$  from  $\vec{x}$ . The value of  $r_m$  is

APPENDIX B

given by  $r_m = \sqrt{r_0^2 + (\xi_0 b)^2 + 2r_0 \xi_0 b \cos \beta}$ . The radius  $r_m$  makes an angle  $\beta_m$  with respect to the  $y_2$ -axis which is related by

$$\cos \beta_m = \frac{r_m^2 + (\xi_0 b)^2 - r_0^2}{2r_m \xi_0 b} \quad (B4)$$

The distance from a point within element  $m$  on the  $y_2$ -axis to  $\vec{x}$  is approximated closely by  $r_m + b(\xi - \xi_0) \cos \beta_m$ . Therefore, the radius  $r_t$  from a point on the top segment to  $\vec{x}$  is

$$r_t \approx r_m + b(\xi - \xi_0) \cos \beta_m - b[\epsilon - \eta(\xi - \xi_0)] \sin \beta_m$$

For the bottom segment this radius is

$$r_b \approx r_m + b(\xi - \xi_0) \cos \beta_m + b[\epsilon - \eta(\xi - \xi_0)] \sin \beta_m$$

Rearranging the expressions for  $r_t$  and  $r_b$  gives

$$\left. \begin{aligned} r_t &= r_m - \frac{k_0}{k} - \frac{\xi_0}{k}(k_x + k_s) + \frac{\xi}{k}(k_x + k_s) \\ r_b &= r_m + \frac{k_0}{k} - \frac{\xi_0}{k}(k_x - k_s) + \frac{\xi}{k}(k_x - k_s) \end{aligned} \right\} \quad (B5)$$

where

$k$  wave number,  $\omega/c$

$k_0 = k b \epsilon \sin \beta_m$

$k_x = k b \cos \beta_m$

$k_s = k b \eta \sin \beta_m$

The cosines of angles  $\tilde{\theta}_t$  and  $\tilde{\theta}_b$  are approximated as follows:

$$\left. \begin{aligned} \cos \tilde{\theta}_t &\approx \frac{\hat{n}_t \cdot \vec{r}_m}{r_m} = -\frac{\eta}{\sqrt{1 + \eta^2}} \cos \beta_m + \frac{1}{\sqrt{1 + \eta^2}} \sin \beta_m \\ \cos \tilde{\theta}_b &\approx \frac{\hat{n}_b \cdot \vec{r}_m}{r_m} = -\frac{\eta}{\sqrt{1 + \eta^2}} \cos \beta_m - \frac{1}{\sqrt{1 + \eta^2}} \sin \beta_m \end{aligned} \right\} \quad (B6)$$

The preceding approximations for  $r_t$ ,  $r_b$ ,  $\cos \tilde{\theta}_t$ , and  $\cos \tilde{\theta}_b$  are valid for each point on the segments because  $l \ll r_m$ , where  $l$  is the airfoil semispan on the  $y_1$ -axis.

For the integrals of equations (B2) and (B3), only first-order approximations are required for  $r_t$  and  $r_b$  in the denominators. These are determined

APPENDIX B

by evaluating the previously obtained values of  $r_t$  and  $r_b$  at the center of each segment, which are defined as  $r_{t,o}$  and  $r_{b,o}$  and are found to be

$$\left. \begin{aligned} r_{t,o} &\approx r_m - \epsilon b \sin \beta_m \\ r_{b,o} &\approx r_m + \epsilon b \sin \beta_m \end{aligned} \right\} \quad (B7)$$

To evaluate equations (B2) and (B3), it is noted that the values obtained for the radii  $r_t$  and  $r_b$  and the angles  $\tilde{\theta}_t$  and  $\tilde{\theta}_b$  are independent of the  $y_1$ -coordinate. Also, the only dependence of these values on the variable  $\xi$  is contained in the last terms of the approximations for  $r_t$  and  $r_b$  in equations (B5). Upon integration and rearrangement, equations (B2) and (B3) become, respectively,

$$\begin{aligned} (\text{SPV})_m &= \frac{-\rho_o \omega^2 \alpha b^2 \lambda (1 - \eta^2) \exp [i(\omega t - kr_m)]}{2\pi} \left\{ \frac{A_m}{(k_x + k_s) r_{t,o}} \right. \\ &\times \left[ 1 + \frac{i(k_x + k_s) \eta (\epsilon + \eta \xi_o)}{1 - \eta^2} \right] - \frac{B_m}{(k_x - k_s) r_{b,o}} \left[ 1 + \frac{i(k_x - k_s) \eta (\epsilon + \eta \xi_o)}{1 - \eta^2} \right] \\ &\left. + \frac{iC_m}{r_{t,o}} - \frac{iD_m}{r_{b,o}} \right\} \quad (B8) \end{aligned}$$

and

$$(\text{SPP})_m = \frac{-P_m k \lambda b \sqrt{1 + \eta^2} \exp [i(\omega t - kr_m)]}{2\pi} \left( \frac{A_m \cos \tilde{\theta}_t}{r_{t,o}} - \frac{B_m \cos \tilde{\theta}_b}{r_{b,o}} \right) \quad (B9)$$

where

$$A_m = \frac{\exp (ik_0)}{k_x + k_s} \left\{ \exp [-i(k_x + k_s)(\xi_2 - \xi_o)] - \exp [-i(k_x + k_s)(\xi_1 - \xi_o)] \right\}$$

$$B_m = \frac{\exp (-ik_0)}{k_x - k_s} \left\{ \exp [-i(k_x - k_s)(\xi_2 - \xi_o)] - \exp [-i(k_x - k_s)(\xi_1 - \xi_o)] \right\}$$

$$C_m = \frac{\exp (ik_0)}{k_x + k_s} \left\{ \xi_2 \exp [-i(k_x + k_s)(\xi_2 - \xi_o)] - \xi_1 \exp [-i(k_x + k_s)(\xi_1 - \xi_o)] \right\}$$

and

$$D_m = \frac{\exp (-ik_0)}{k_x - k_s} \left\{ \xi_2 \exp [-i(k_x - k_s)(\xi_2 - \xi_o)] - \xi_1 \exp [-i(k_x - k_s)(\xi_1 - \xi_o)] \right\}$$

These equations, when applied to equation (7), render the prediction of the sound field as based on the airfoil equivalent model shown in figure 8(b). Equations (B8) and (B9) are calculated by using experimental results of table 1 and the coordinates and slopes of the airfoil equivalent model given in table B1. The prediction ignores the near-field term of equation (5). This term is easily accounted for in equation (B9) by multiplying  $A_m$  by the factor  $1 + (1/ikr_{t,o})$

## APPENDIX B

and  $B_m$  by the factor  $1 + (1/ikr_{b,o})$ . However, the contribution of these factors is small because the observer at  $\vec{x}$  is considered in the far field of the element  $m$ .

A more approximate theoretical model is obtained when one assumes that the airfoil thickness is zero (fig. 8(c)), in which case the values of  $\epsilon$  and  $\eta$  of equation (B1) become zero; this requires  $k_0 = k_s = 0$ ,  $\cos \tilde{\theta}_t = -\cos \tilde{\theta}_b$ ,  $r_{t,o} = r_{b,o} = r_m$ ,  $A_m = B_m$ , and  $C_m = D_m$ . As a result, the contribution from the  $(SPV)_m$  term in equation (B8) is zero.

In addition to the preceding approximation in regard to thickness, if the value of  $k_x$  multiplied by the width of the element  $\xi_2 - \xi_1$  is small, then the terms  $A_m$  and  $B_m$  each approach the value  $-i(\xi_2 - \xi_1)$ . The total force on the element  $m$  is  $2P_m(2\ell)(\xi_2 - \xi_1)b \equiv F_m$ ; substituting this value in equation (B9) gives

$$(SPP)_m = \frac{iF_mk \cos \tilde{\theta}_t}{4\pi r_m} \exp \left[ i\omega \left( t - \frac{r_m}{c} \right) \right] \quad (B10)$$

Now if the previously mentioned near-field factors are inserted, equation (B10) becomes

$$(SPP)_m = \frac{F_m \cos \tilde{\theta}_t \exp \left[ i\omega \left( t - \frac{r_m}{c} \right) \right]}{4\pi r_m} \left( ik + \frac{1}{r_m} \right)$$

which represents the sound radiated by a simple dipole.

## APPENDIX C

### ERROR ANALYSIS

In order to evaluate the accuracy of the comparisons between theoretical and experimental results in figures 9 and 10, one can examine the individual experimental and theoretical components and their contribution to the comparisons.

#### Experimental Accuracy

The expected accuracy of the experimental noise data can be determined from the results of the acoustic field test in figure 5. The figure shows a scatter error of  $\pm 1$  dB in sound pressure level and  $\pm 12^\circ$  in phase for 14 of the 16 independent microphone systems.

The accelerometer measurements are predicted to be accurate within 6 percent. This would correspond to an error of  $\pm 0.5$  dB in level for the calculated contribution of the surface-velocity term (eq. (8)) to the noise prediction equation. As will be shown in this appendix, the contribution of the surface-velocity term is very small compared with that of the surface-pressure term (eq. (9)). Therefore, any expected accelerometer measurement error contributes very little to the experimental-theoretical comparisons.

The surface-pressure transducers were found to give very repeatable calibration and pressure measurement results. In determining a reasonable error band for the pressure data, one may look to differences found between transducers in regard to the sensitivity ratio  $S_a/S_p$ , defined in equation (6). On the basis of calculations made by using the standard deviation of the calibrated values of  $S_a/S_p$ , the expected error is less than  $\pm 0.6$  dB in surface pressure level and less than  $\pm 1.0^\circ$  in phase for any datum point of figure 6. By using this error band, an analysis of conceivable error buildup in the prediction of the sound field renders an expected error band of  $\pm 1.2$  dB in sound pressure level and  $\pm 10^\circ$  in phase for the theoretical curves of figures 9 and 10.

#### Model Accuracy

The effect of the degree of theoretical-model refinement was examined and some results are shown in figure C1. In this figure various predictions, based on model refinements of figure 8, are given of sound pressure level and phase as a function of directivity angle  $\beta$  for two of the experimental cases. No experimental noise data are shown.

It is seen that the predictions using the airfoil equivalent model, used for the theoretical curves of figures 9 and 10, are closely approximated by using a model with assumed zero airfoil thickness in noise calculations. With zero thickness, the value of equation (8) reduces to zero and that of equation (9) increases slightly; this renders a total prediction reduction of only about 0.5 dB in sound pressure level and a change in phase of less than  $2.0^\circ$ .

## APPENDIX C

This shows that for the experimental cases considered in this study, airfoil contour refinement may be regarded as unnecessary.

An even more approximate prediction is obtained when the airfoil is replaced by two simple dipoles whose strength is determined by summing measurements over the surface and whose positions are specified near the centroids of the in-phase regions (fig. 8(d)). The calculated results for three values of the angle  $\beta$  are shown in figure C1 for the two-dipole approximation and are seen to be within 1.5 dB of the values for the more exact models.

The effect on prediction of increasing the number of radiating elements beyond eight was examined. It was found that for surface-pressure distributions similar to those of figure 6, additional refinement incorporating more elements could result in changes of only about 0.1 dB in predicted noise level. Therefore, for the cases considered, eight theoretical model elements are sufficient for accurate prediction.

Spanwise compactness is assumed in the model and is allowed because of the acoustic-field measuring positions, which were in the plane perpendicular to the airfoil surface at the midspan. Analysis has determined that the maximum expected error due to this assumption would be a negligible difference of  $10^{-3}$  dB in sound pressure level and less than  $1^\circ$  in phase.

Also, as previously mentioned, there was 0.7 dB subtracted from the theoretical values of figures 9 and 10 to account for spanwise diminishing levels near the airfoil edges. This should be an accurate adjustment within 0.1 dB, assuming the spanwise level continues to drop near the edge in the manner indicated in figure 7.

## REFERENCES

1. Baker, Bevan B.; and Copson, E. T.: The Mathematical Theory of Huygens' Principle. Second ed. Oxford Univ. Press, 1969, pp. 1-44.
2. Curle, N.: The Influence of Solid Boundaries Upon Aerodynamic Sound. Proc. R. Soc. (London), ser. A, vol. 231, no. 1187, Sept. 20, 1955, pp. 505-514.
3. Lighthill, M. J.: On Sound Generated Aerodynamically. I. General Theory. Proc. R. Soc. (London), vol. 211, no. 1107, Mar. 20, 1952, pp. 564-587.
4. Ffowcs Williams, J. E.; and Hawkings, D. L.: Sound Generation by Turbulence and Surfaces in Arbitrary Motion. Philos. Trans. R. Soc. London, ser. A, vol. 264, no. 1151, May 8, 1969, pp. 321-342.
5. Amiet, R. K.: Acoustic Radiation From an Airfoil in a Turbulent Stream. J. Sound & Vib., vol. 41, no. 4, Aug. 1975, pp. 407-420.
6. Sharland, I. J.: Sources of Noise in Axial Flow Fans. J. Sound & Vib., vol. 1, no. 3, July 1964, pp. 302-322.
7. Morse, Philip M.; and Ingard, K. Uno: Theoretical Acoustics. McGraw-Hill Book Co., Inc., c.1968, p. 321.
8. Richards, E. J.; and Mead, D. J., eds.: Noise and Acoustic Fatigue in Aeronautics. John Wiley & Sons, Ltd., 1968.
9. Farassat, F.: Theory of Noise Generation From Moving Bodies With an Application to Helicopter Rotors. NASA TR R-451, 1975.
10. Farassat, F.; and Brown, T. J.: Development of a Noncompact Source Theory With Applications to Helicopter Rotors. AIAA Paper No. 76-563, 1976.
11. Clark, P. J. F.; and Ribner, H. S.: Direct Correlation of Fluctuating Lift With Radiated Sound for an Airfoil in Turbulent Flow. J. Acoust. Soc. America, vol. 46, no.3, Sept. 1969, pp. 802-805.
12. Paterson, Robert W.; and Amiet, Ray K.: Acoustic Radiation and Surface Pressure Characteristics of an Airfoil Due to Incident Turbulence. AIAA Paper No. 76-571, July 1976.
13. Farassat, F.; and Brown, T. J.: A New Capability for Predicting Helicopter Rotor and Propeller Noise Including the Effect of Forward Motion. NASA TM X-74037, 1977.
14. Hanson, Donald B.: Near Field Noise of High Tip Speed Propellers in Forward Flight. AIAA Paper No. 76-565, July 1976.
15. Hardin, Jay C.: Airframe Self-Noise - Four Years of Research. Aerodynamic Noise, AGARD-LS-80, Jan. 1977, pp. 6-1 - 6-19.

16. Commerford, G. L.; and Carta, F. O.: An Exploratory Investigation of the Unsteady Aerodynamic Response of a Two-Dimensional Airfoil at High Reduced Frequency. AIAA Paper No. 73-309, Mar. 1973.
17. IS Pressure Transducers. LQ Series - Thin Line Design. Bull. KPS-LQ3 Ser., Kulite Semiconductor Products, Inc.
18. Norum, Thomas D.: Measured and Calculated Transmission Losses of Sound Waves Through a Helium Layer. NASA TN D-7230, 1973.
19. Satyanarayana, B.; and Davis, Sanford: Experimental Studies of Trailing-Edge Conditions on an Oscillating Airfoil at Frequency Parameters of Up to One. AIAA Paper No. 77-450, Mar. 1977.
20. Archibald, F. S.: Unsteady Kutta Condition at High Values of the Reduced Frequency Parameter. J. Aircr., vol. 12, no. 6, June 1975, pp. 545-500.
21. Yates, John E.: On the Singular Role of Viscosity in the Theory of Thin Airfoils. Rep. 306 (Contract N00014-76-C-0576), Aeronaut. Res. Assoc. Princeton, Inc., May 1977.
22. Stratton, Julius Adams: Electromagnetic Theory. McGraw-Hill Book Co., Inc., 1941, pp. 424-428, 460-464.
23. Lamb, Horace: Hydrodynamics. Sixth ed. Cambridge Univ. Press, 1932, pp. 498-502.
24. Skudrzyk, Eugen: The Foundations of Acoustics. Springer-Verlag, 1971, pp. 489-500.
25. Malecki, I. (Irena Bellert, transl.): Physical Foundations of Technical Acoustics. Pergamon Press, Inc., c.1969, pp. 149-162.

TABLE 1.- TEST CONDITIONS AND SURFACE PRESSURE RESULTS<sup>a</sup>

Transducer number	Transducer location, percent chord	f = 301 Hz; $\alpha = 82.1 \mu\text{rad}$		f = 301 Hz; $\alpha = 259.3 \mu\text{rad}$		f = 477 Hz; $\alpha = 30.8 \mu\text{rad}$		f = 477 Hz; $\alpha = 97.6 \mu\text{rad}$	
		Peak pressure, $ P_m $ , Pa	Phase, $\varphi_p - \varphi_a$ , <sup>b</sup> deg	Peak pressure, $ P_m $ , Pa	Phase, $\varphi_p - \varphi_a$ , <sup>b</sup> deg	Peak pressure, $ P_m $ , Pa	Phase, $\varphi_p - \varphi_a$ , <sup>b</sup> deg	Peak pressure, $ P_m $ , Pa	Phase, $\varphi_p - \varphi_a$ , <sup>b</sup> deg
1	1.4	5.77	356	24.47	356	7.65	3	22.73	4
2	9.7	5.63	359	21.36	355	6.17	0	19.53	0
3	21.2	5.31	359	21.35	355	6.64	6	20.43	6
4	31.9	1.58	0	7.42	343	3.09	22	9.26	23
5	48.6	2.91	161	11.14	169	3.01	139	9.62	140
6	61.8	6.44	164	26.27	175	7.34	171	23.53	171
7	78.1	9.49	164	37.93	175	11.03	170	34.88	170
8	88.9	10.39	162	40.26	176	11.96	171	38.34	173

<sup>a</sup>Terminology consistent with that of equation (B9).

<sup>b</sup> $\varphi_p - \varphi_a$  is the phase by which the surface pressure leads the normal surface acceleration near airfoil leading edge.

TABLE B1.- CONSTANTS FOR EQUATIONS (B8) AND (B9)

(a) Physical and geometric constants

Semichord, $b$ , m (ft) . . . . .	0.2286 (0.750)
Semispan, $l$ , m (ft) . . . . .	0.1524 (0.500)
Measurement radius, $r_0$ , m (ft) . . . . .	2.21 (7.25)
Speed of sound, $c$ , m/s (ft/sec) . . . . .	344 (1130)
Mean air density, $\rho_0$ , kg/m <sup>3</sup> (lbm/ft <sup>3</sup> ) . . . . .	1.20 (0.075)
Acceleration due to gravity, $g$ , m/s <sup>2</sup> (ft/sec <sup>2</sup> ) . . . . .	9.8066 (32.174)

(b) Coordinates and slopes of airfoil equivalent model

Element number, $m$	Transducer location, percent chord	$\epsilon$	$\eta$	$\xi_2$	$\xi_1$
1	1.4	0.055	-0.600	-0.722	-0.833
2	9.7	.100	-.111	-.522	-.722
3	21.2	.117	-.050	-.300	-.522
4	31.9	.116	.040	-.022	-.300
5	48.6	.106	.038	.273	-.023
6	61.8	.085	.101	.569	.273
7	78.1	.058	.094	.843	.569
8	88.9	.022	.137	1.166	.843

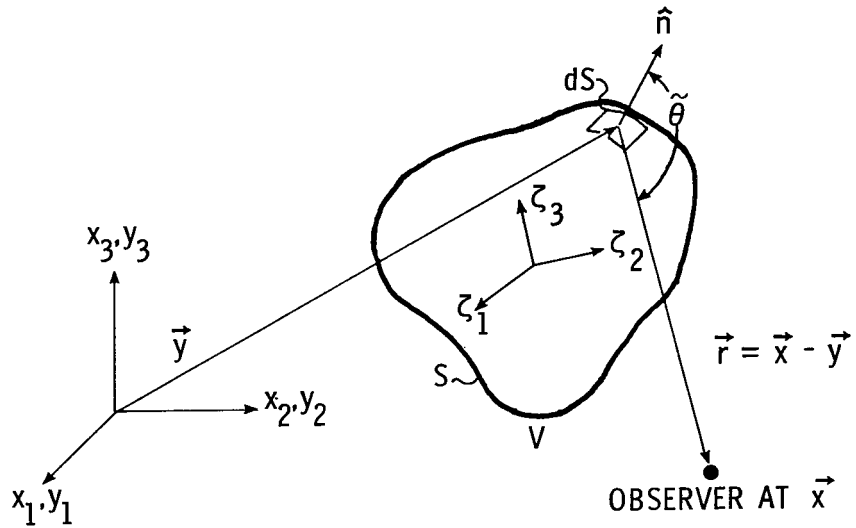


Figure 1.- Coordinate systems and integration region for equations (1) and (4).

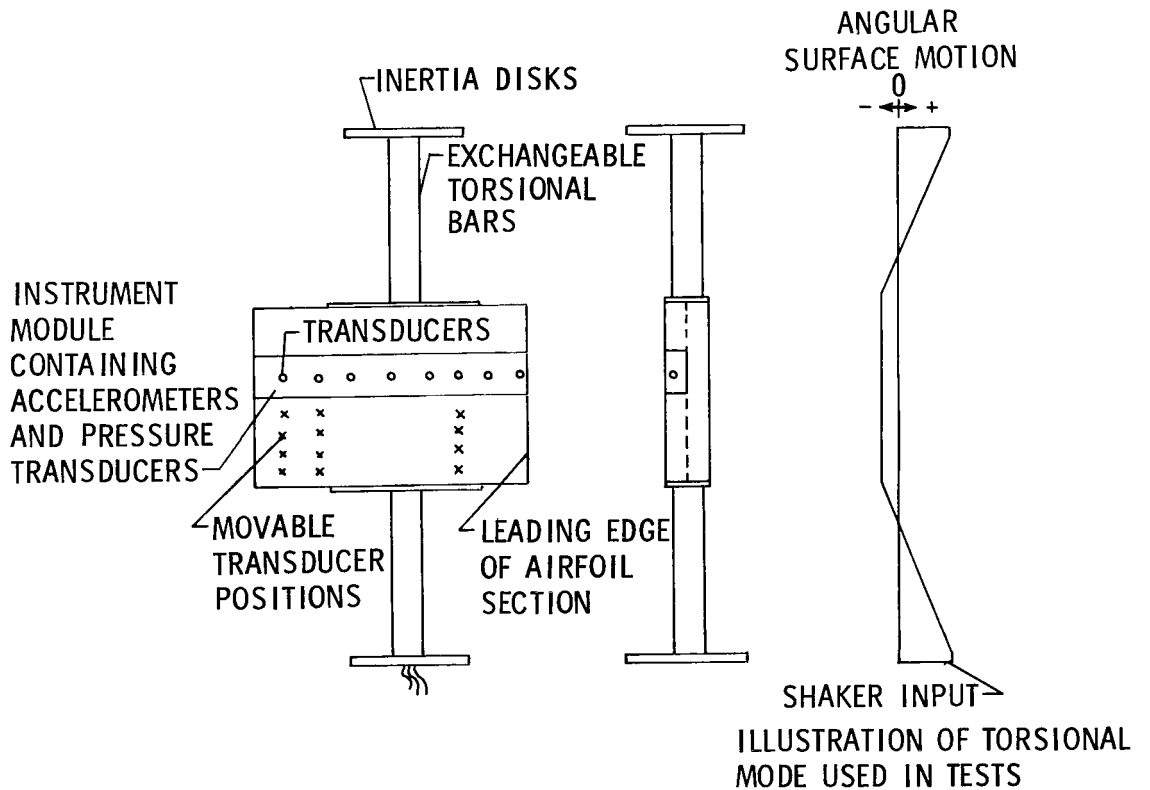
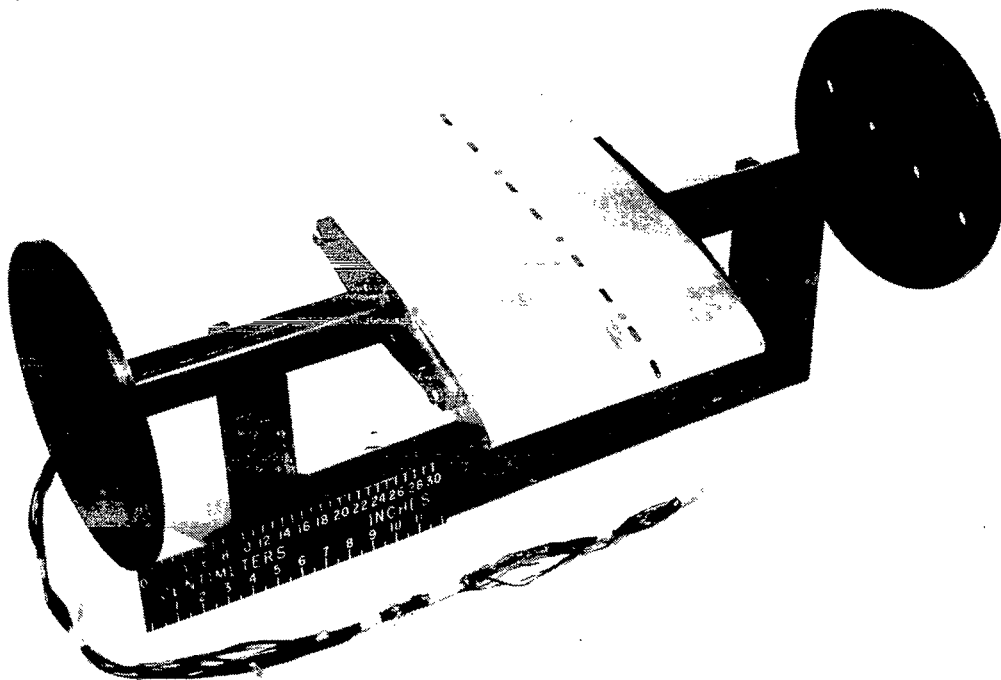


Figure 2.- Experimental model with illustration of torsional mode employed in tests.



L-75-3694

Figure 3.- Experimental model in the 301-Hz configuration.

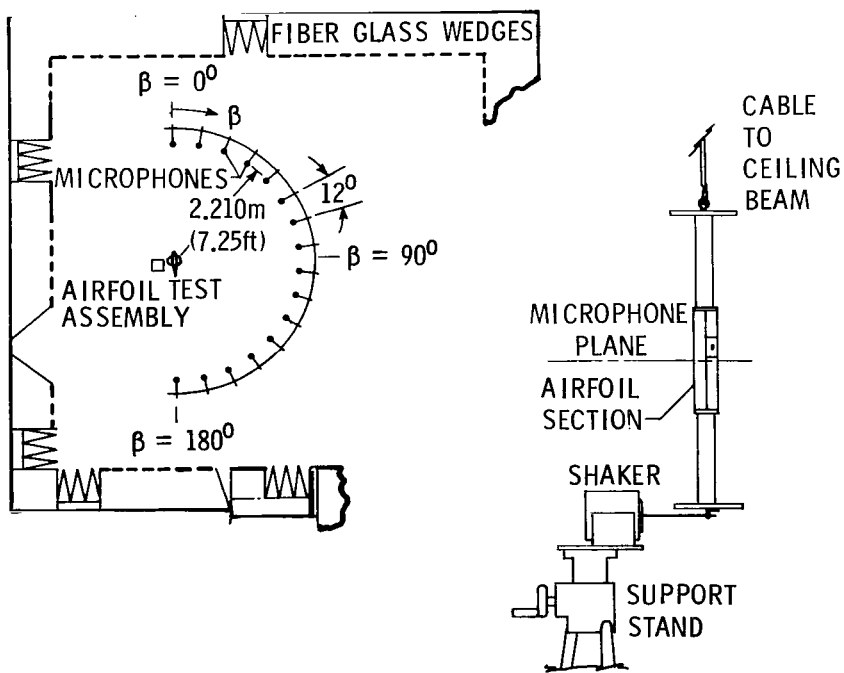


Figure 4.- Plan view of airfoil test assembly in anechoic chamber and side view of assembly.

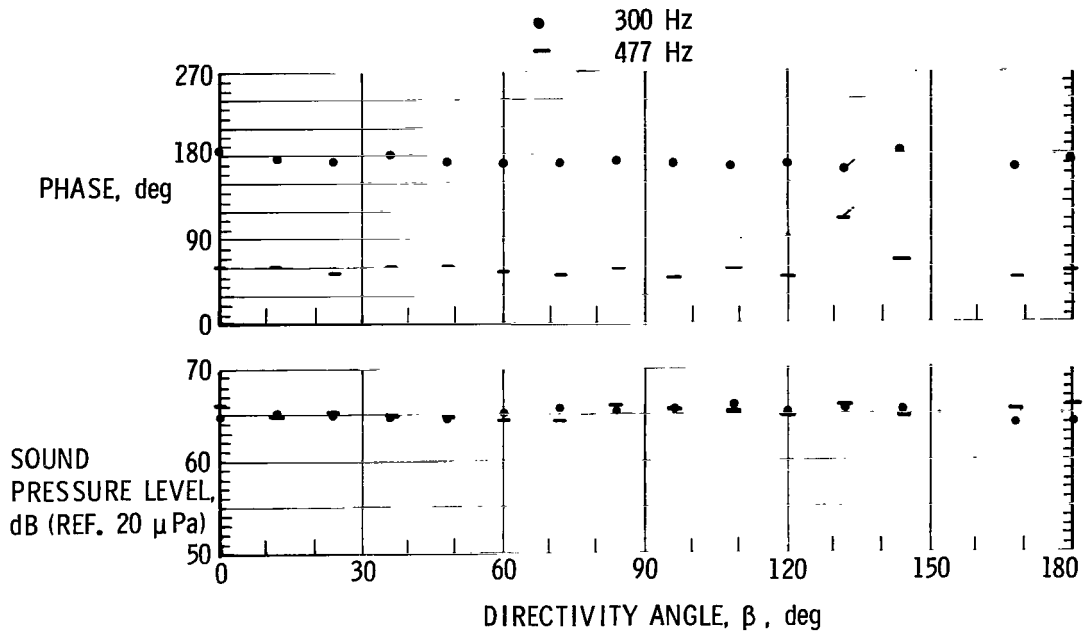


Figure 5.- Results of acoustic field test for the microphones all at a radius of 2.210 m (7.25 ft) from simple source at airfoil location (airfoil removed).

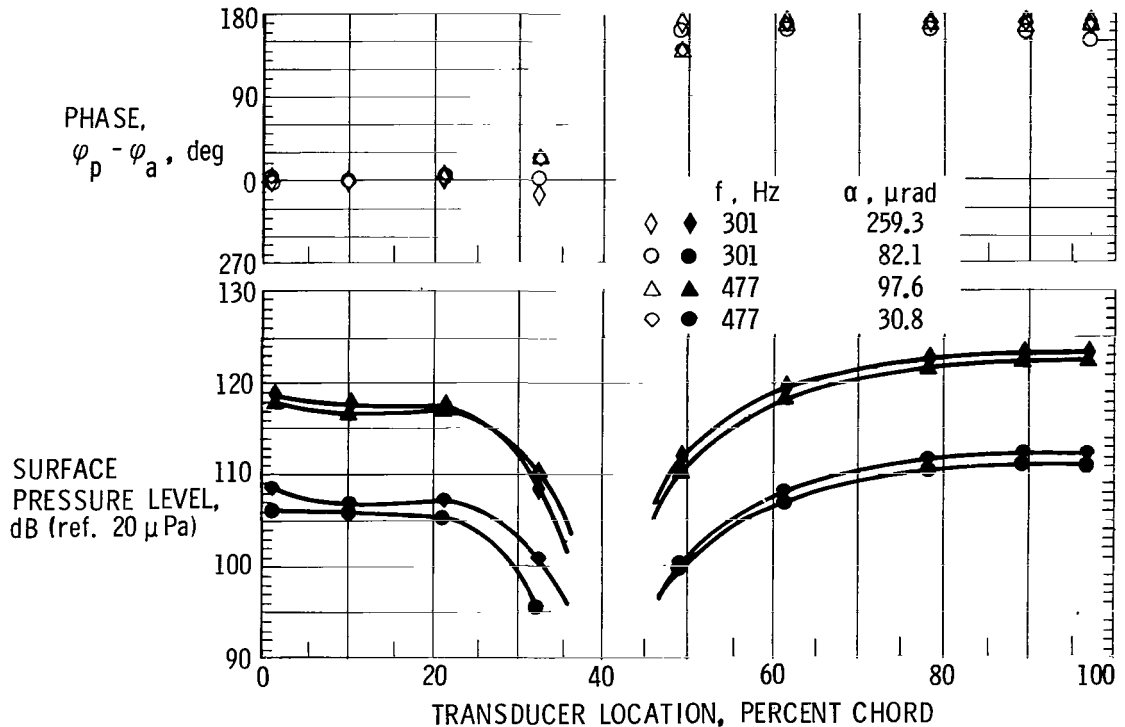


Figure 6.- Surface pressure level and phase as a function of transducer location. Chord length: 45.72 cm (18.0 in.).

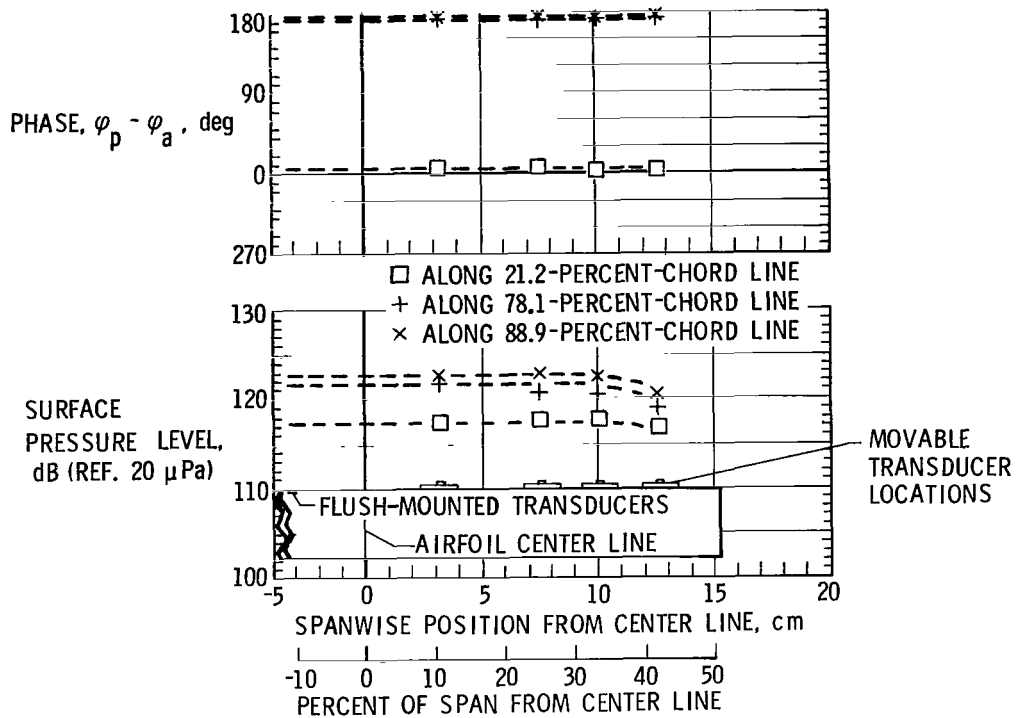


Figure 7.- Results of spanwise pressure survey - surface pressure level and phase as a function of spanwise location for  $f = 477$  Hz. Airfoil span: 30.48 cm (12.0 in.).

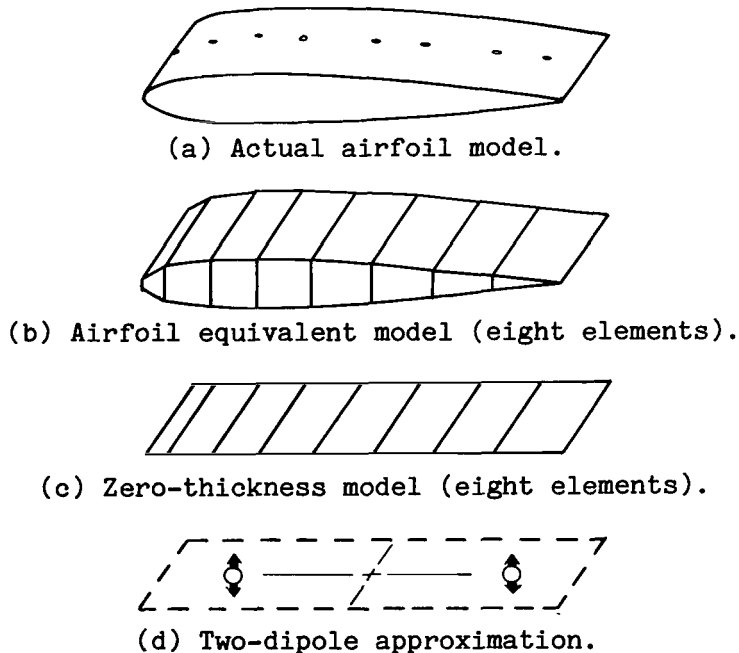


Figure 8.- Illustrations of actual model and theoretical models used in the investigation.

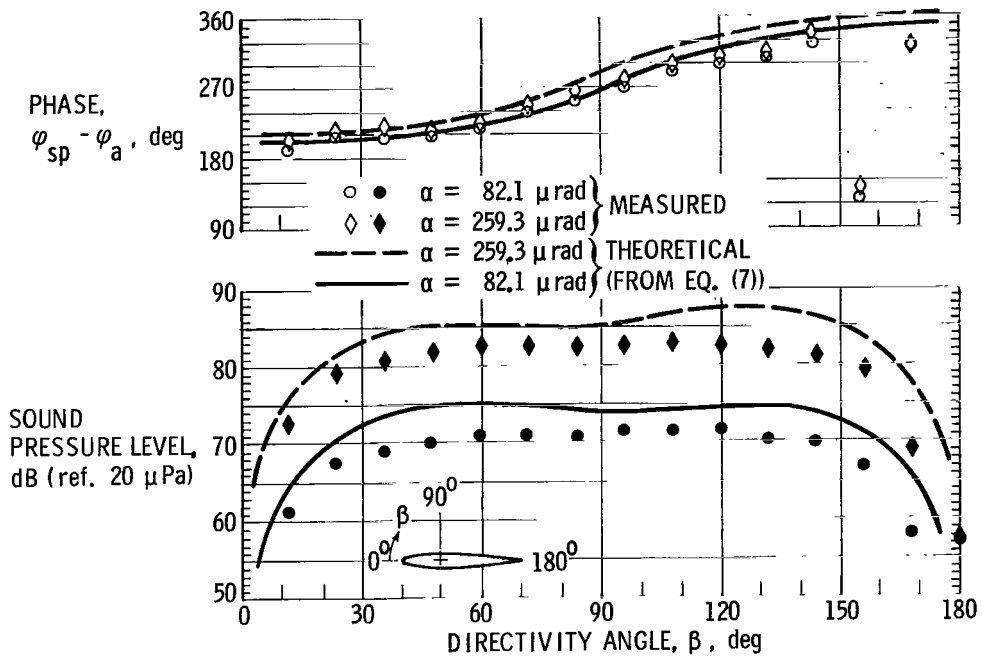


Figure 9.- Sound pressure level and phase as a function of directivity angle  $\beta$  at a measurement radius of 2.210 m (7.25 ft) for airfoil oscillating at  $f = 301$  Hz.

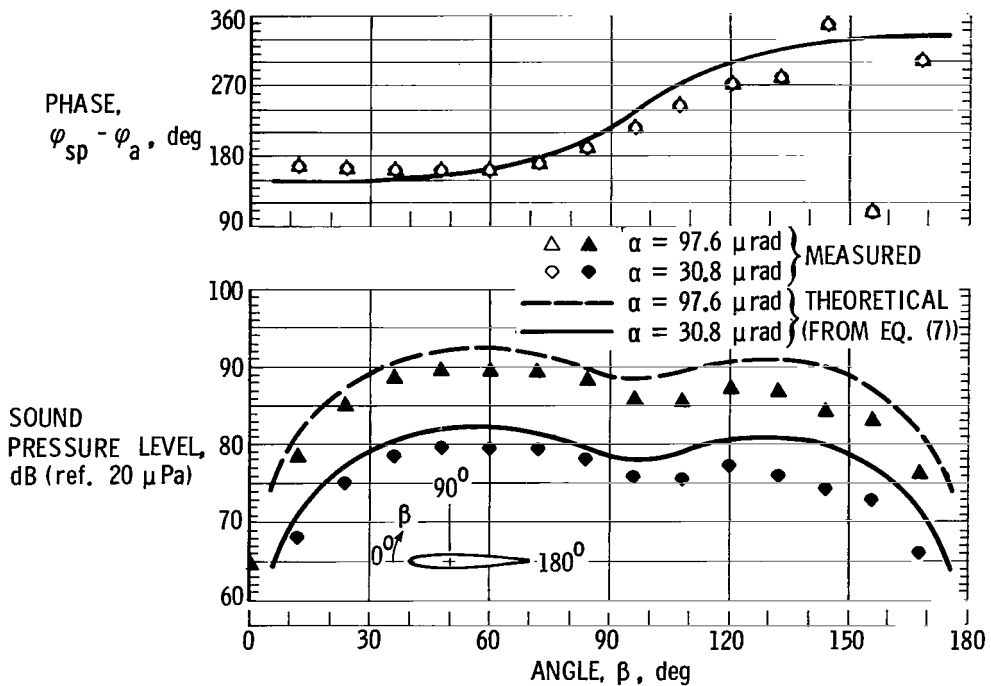


Figure 10.- Sound pressure level and phase as a function of directivity angle  $\beta$  at a measurement radius of 2.210 m (7.25 ft) for airfoil oscillating at  $f = 477$  Hz.

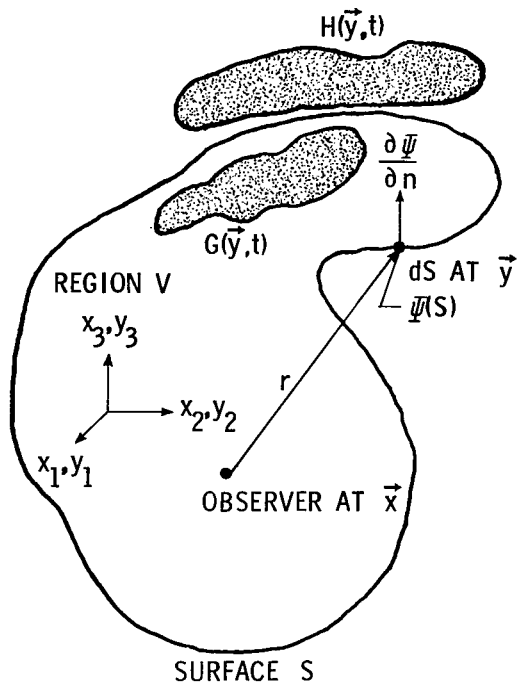


Figure A1.- Integration region for Kirchhoff formula.

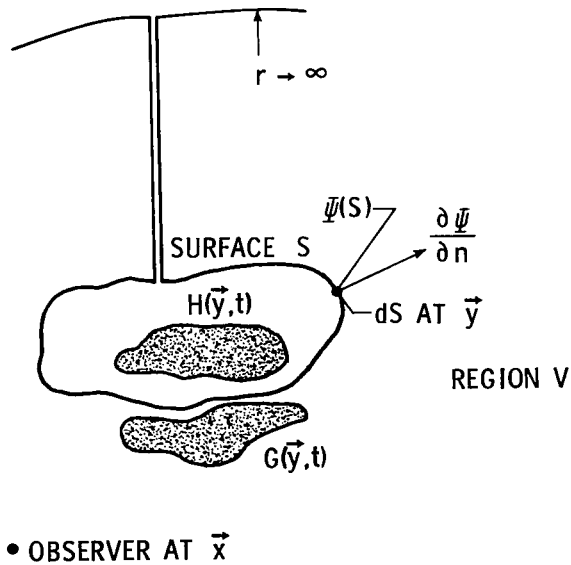


Figure A2.- Integration region for Kirchhoff formula when region V is bounded internally by surface S.

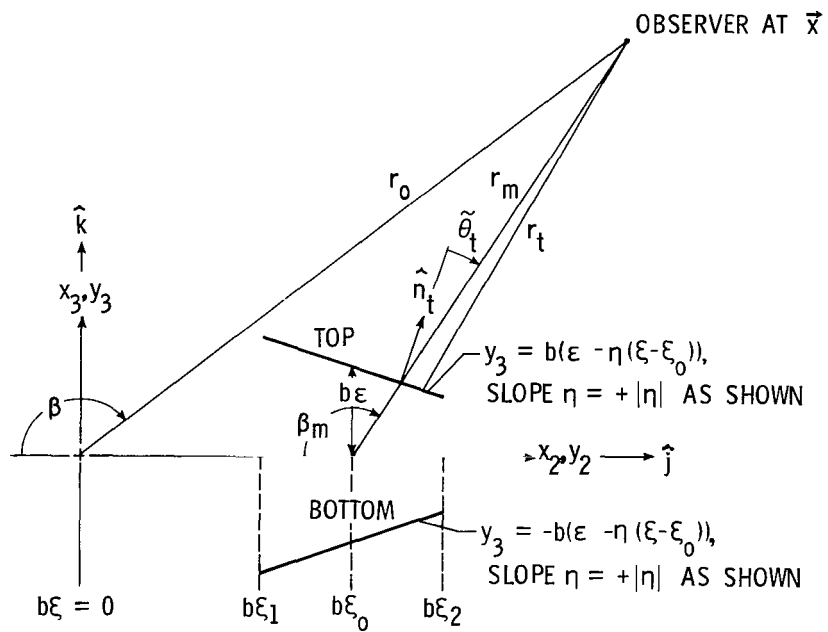


Figure B1.- Coordinate system used in development of sound field formulation of an airfoil equivalent element.

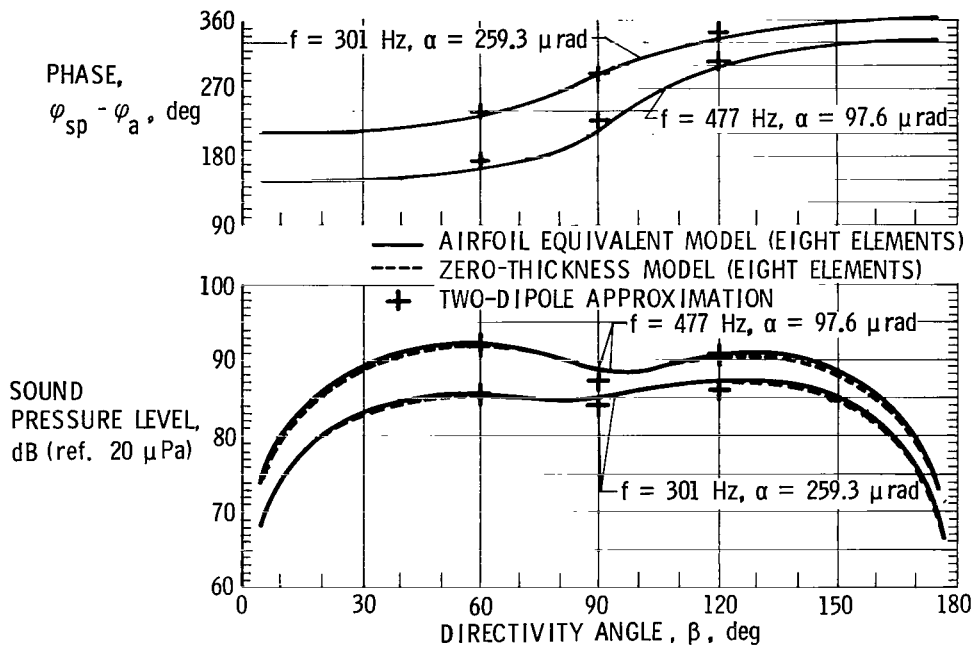


Figure C1.- Predicted values obtained by using various acoustic models for two of the cases considered in the study (no experimental noise data shown).

1. Report No. NASA TP-1048		2. Government Accession No.		3. Recipient's Catalog No.	
4. Title and Subtitle AN EXPERIMENTAL EVALUATION OF THE APPLICATION OF THE KIRCHHOFF FORMULATION FOR SOUND RADIATION FROM AN OSCILLATING AIRFOIL				5. Report Date December 1977	
				6. Performing Organization Code	
7. Author(s) Thomas F. Brooks				8. Performing Organization Report No. L-11479	
9. Performing Organization Name and Address NASA Langley Research Center Hampton, VA 23665				10. Work Unit No. 505-03-11-04	
				11. Contract or Grant No.	
12. Sponsoring Agency Name and Address National Aeronautics and Space Administration Washington, DC 20546				13. Type of Report and Period Covered Technical Paper	
				14. Sponsoring Agency Code	
15. Supplementary Notes					
16. Abstract <p>The Kirchhoff integral formulation, which is often applied in aeroacoustic problems involving radiation from surfaces, is evaluated for its effectiveness in quantitatively predicting the sound radiated from an oscillating airfoil whose chord length is comparable with the acoustic wavelength. A rigid airfoil section was oscillated at small amplitude in a medium at rest to produce the sound field. Simultaneous amplitude and phase measurements were made of surface-pressure and surface-velocity distributions and the acoustic free field. Measured surface pressure and motion are used in applying the theory, and airfoil thickness and contour are taken into account. The result of the investigation was that theory overpredicted the sound pressure level by 2 to 5 dB, depending on direction. Differences were also noted in the sound-field phase behavior.</p>					
17. Key Words (Suggested by Author(s)) Aeroacoustics Aerodynamic noise Linear and physical acoustics				18. Distribution Statement Unclassified - Unlimited	
				Subject Category 71	
19. Security Classif. (of this report) Unclassified		20. Security Classif. (of this page) Unclassified		21. No. of Pages 37	22. Price* \$4.00

National Aeronautics and  
Space Administration

THIRD-CLASS BULK RATE

Postage and Fees Paid  
National Aeronautics and  
Space Administration  
NASA-451



Washington, D.C.  
20546

Official Business

Penalty for Private Use, \$300

15 1 1U,H, 112877 S00903DS  
DEPT OF THE AIR FORCE  
AF WEAPONS LABORATORY  
ATTN: TECHNICAL LIBRARY (SUL)  
KIRTLAND AFB NM 87117

**NASA**

---

POSTMASTER: If Undeliverable (Section 158  
Postal Manual) Do Not Return